

# Determination of the Effective Inelastic $p\bar{p}$ Cross-Section for the DØ Run II Luminosity Measurement

Tamsin Edwards, Sahal Yacoob, Tim Andeen,  
Michael Begel, Brendan Casey, Rich Partridge, Heidi Schellman, Andre Sznajder

We determine the effective inelastic  $p\bar{p}$  cross-section into the DØ Luminosity Monitor for all run periods prior to September 2004. This number is used to relate the measured inelastic collision rate to the delivered luminosity. The key ingredients are the inelastic  $p\bar{p}$  cross-section, the Luminosity Monitor efficiency, and the modeling of kinematic distributions for various inelastic processes used to determine the detector acceptance. The resulting value is  $\sigma_{p\bar{p},\text{eff}} = 46 \pm 3$  mb.

## I. INTRODUCTION

The DØ detector [1] is a multi-purpose magnetic spectrometer and calorimeter operating at the Fermilab Tevatron  $p\bar{p}$  collider at a center-of-mass energy  $\sqrt{s} = 1.96$  TeV. The detector is designed to discover and measure the production cross-sections for exotic phenomena and to make precision cross-section measurements for several standard model processes [2]. An essential ingredient in all DØ cross-section measurements is the integrated beam luminosity used to normalize the data sample. We determine the instantaneous luminosity,  $\mathcal{L}$ , by measuring the rate of inelastic  $p\bar{p}$  collisions recorded by the DØ Luminosity Monitor(LM) [3]

$$\mathcal{L} = \frac{1}{\sigma_{p\bar{p},\text{eff}}} \frac{dN}{dt}(p\bar{p})$$

where  $\sigma_{p\bar{p},\text{eff}}$  is the effective inelastic  $p\bar{p}$  cross-section into the LM related to the inelastic cross-section by

$$\sigma_{p\bar{p},\text{eff}} = \epsilon \times A \times \sigma_{p\bar{p}}.$$

The acceptance,  $A$ , takes into account the probability for an interaction to have particles in the geometric coverage of the LM and the efficiency,  $\epsilon$ , is the probability that an event will be recorded by the detector given that particles are in the detector acceptance.

Here, we will follow closely the procedures successfully employed by DØ in the Tevatron Run I to determine the effective cross-section [4,5]. After a brief overview of the LM, we discuss the inelastic cross-section, followed by the acceptance and efficiency determinations. Corrections applied to account for beam-induced background are also discussed.

## II. LUMINOSITY MONITOR

The LM (Fig. 1) consists of two arrays of 24 plastic scintillator wedges arranged azimuthally around the beam pipe located at  $z = \pm 140$  cm where the positive  $z$  axis is aligned with the proton beam. North is in the negative  $z$  direction. The arrays cover the pseudo-rapidity region  $2.7 < |\eta| < 4.4$ . The detector components are immersed in a 1 T axial magnetic field.

A schematic of the signal processing is shown in Fig. 2. Each scintillator is read out using a fine-mesh PMT. The PMT signals from the 24 counters in each array are summed and the sum is discriminated to give single timing pulses for the north and south arrays,  $T_N$  and  $T_S$ . The time pulses are fed into a custom FASTZ vertex module that determines the vertex,  $z_{vtx}$ , using the time difference between the arrays

$$z_{vtx} = \frac{c}{2}(T_S - T_N).$$

The resolution on  $z_{vtx}$  is approximately 6 cm.

As shown in Fig. 3, particles generated by a  $p\bar{p}$  collision occurring in the interaction region will have nearly equal time-of-flight (TOF) to the north and south arrays leading to a  $z_{vtx}$  distribution centered at  $z = 0$  cm. The distribution is a Gaussian with  $\sigma \sim 30$  cm determined by the size of  $D\bar{O}$  interaction region. Beam induced background interactions that occur upstream of the  $D\bar{O}$  detector are referred to as beam halo. Halo particles hit one array and traverse the  $D\bar{O}$  interaction region before hitting the other array leading to a large TOF difference between the two arrays and  $z_{vtx}$  distributions centered at  $-140$  cm for proton halo interactions and  $+140$  cm for anti-proton halo interactions.

We require inelastic collisions to have a vertex reconstructed within  $|z_{vtx}| < 97$  cm,  $\bar{p}$  halo events to have  $116 < z_{vtx} < 166$  cm, and  $p$  halo events to have  $-166 < z_{vtx} < -116$  cm. Events that do not pass these requirements are not recorded. For events passing one of the requirements, the  $z_{vtx}$ , event classification, and discriminator logic levels for the north and south arrays are recorded.

### III. INELASTIC CROSS-SECTION

The inelastic  $p\bar{p}$  cross-section has been measured at  $\sqrt{s} = 1.8$  TeV to be  $56.6 \pm 2.2$  mb by the E710 collaboration [6],  $56.5 \pm 1.2$  mb by the E811 collaboration [7], and  $61.7 \pm 1.4$  mb by the CDF collaboration [8]. While the E710 and E811 measurements are in good agreement, the E811 and CDF measurements disagree by 9.2% or  $2.8\sigma$ . By convention, the CDF and  $D\bar{O}$  collaborations use an average value of  $\sigma_{p\bar{p}} = 59.23 \pm 2.3$  mb at  $\sqrt{s} = 1.8$  TeV that has been scaled to a value of  $\sigma_{p\bar{p}} = 60.7 \pm 2.4$  mb at  $\sqrt{s} = 1.96$  TeV [9]. We note that other averaging techniques [10] would shift the central value by 3% and increase the error by a factor of 1.2.

### IV. ACCEPTANCE

#### A. Non-Diffractive and Diffractive Acceptances

We divide inelastic collisions into three processes, non-diffractive or hard-core scattering (HC), single diffractive dissociation of either a proton or anti-proton (SD), and double diffractive dissociation of both the proton and anti-proton (DD). The LM acceptances for these processes are determined using Monte Carlo (MC) simulation. We generate the three topologies with four separate generators [11], Pythia [12,13], MBR [8], PHOJET [14], and DTUJET [15]. The choice of parameters has been optimized to match several kinematic distributions of inclusive inelastic events at the Tevatron [16]. Kinematic distributions for final state particles from Pythia and PHOJET are shown in Figs. 4 to 7. In particular, the SD events are modeled as

$$\frac{d\sigma}{dM^2} \sim \left( \frac{1}{M^2} \right)^\alpha$$

where  $M$  is the invariant mass of the dissociated system, and  $\alpha \sim 1$  for both Pythia and PHOJET, confirmed by fits displayed in Fig. 8. E710 has measured  $\alpha = 1.13 \pm 0.07$  in  $p\bar{p}$  collisions at  $\sqrt{s} = 1.8$  TeV [18] indicating that the Pythia and PHOJET results may be slightly harder than actual diffractive events.

TABLE I. Pythia generator level acceptances for each inelastic process as defined in the text.

Final state	In north Acc.	In south Acc.	Gen level Acc.
hard core	0.971	0.971	0.943
$p + X$ single diffractive	0.265	0.650	0.237
$\bar{p} + X$ single diffractive	0.650	0.253	0.221
double diffractive	0.570	0.579	0.321

The acceptance is defined as the fraction of generated events that have at least one charged particle in the range  $2.7 < \eta < 4.4$  and at least one in the range  $-4.4 < \eta < -2.7$ . The acceptances are listed in Tables I and II. DTUJET gives a much lower value for the SD acceptance. This is expected since PHOJET has been extended to include interaction diagrams that lead to higher-mass diffractive events [17]. Pythia gives a much lower acceptance for DD events, however, there is uncertainty in the distinction between soft HC and DD topologies. The larger HC acceptance for Pythia may indicate that the harder DD components have been classified as HC events by Pythia. This can also be seen in the relative agreements in the total inelastic acceptances determined by weighting each process with its cross-section.

TABLE II. Generator level acceptances for several generators for each inelastic process as defined in the text.

Final state	MBR	PHOJET	DTUJET	Pythia
HC	0.911	0.924	0.949	0.943
SD	0.183	0.280	0.088	0.242
DD	0.563	0.570	0.642	0.321
inelastic	0.75	0.78	0.78	0.76

The Pythia acceptances after the the particles are passed through a GEANT [19] based detector simulator are listed in Table III. We have performed a detailed comparison of the material in the GEANT detector model with the existing engineering drawings and added components when necessary, particularly bellows and flanges that join the Be beam pipe to the Al beam pipe. To estimate the maximum effects of any material not accounted for in the detector model, we regenerate the above MC data sets with the Be beam pipe replaced with a Uranium beam pipe. This procedure was found to reproduce the multiplicity spectrum observed in the Run I LØ detector which was the predecessor of the LM. The nominal and extreme acceptances differ by approximately half a percent. The good agreement between the two material models indicates that the most significant material has been included and the addition of further radiation lengths would have little effect on the results for the acceptance.

TABLE III. Acceptance for Pythia events passed through the GEANT based detector simulator.

Final state	In north Acc.	In south Acc.	Acc.
HC	0.997	0.996	0.994
$p + X$ SD	0.396	0.770	0.390
$\bar{p} + X$ SD	0.768	0.377	0.372
DD	0.742	0.732	0.559

The MBR generator output has been run through a parameterized MC that includes the magnetic field and 0.89 radiation lengths of material [11]. These are compared to the Pythia results in Table IV. The final acceptance is the average of MBR and Pythia results. The generator level PHOJET results are similar to MBR for HC and DD and similar to Pythia for SD events. Therefore the three models are well represented by the average of the MBR and Pythia measurements.

Due to the good agreement between all generators with respect to the acceptance for HC processes, we conclude that an error of plus or minus half the difference between the MBR and Pythia results encompasses all probable models of HC interactions. However, due to the large spread in results for both SD and DD processes, we could expect a spread larger than the difference between the MBR and Pythia results. We therefore apply an error of plus or minus the difference between the MBR and Pythia results.

TABLE IV. Comparison of the Pythia and MBR acceptances. The Pythia events are passed through a GEANT based simulator. The MBR events are passed through a parameterized simulator.

Final state	Pythia	MBR	Final
HC	0.994	0.969	$0.982 \pm 0.013$
SD	0.381	0.244	$0.313 \pm 0.137$
DD	0.559	0.698	$0.624 \pm 0.130$

### B. Combined Acceptance

The cross-sections for the inelastic processes are given in Table V. The single diffractive cross-section is taken from [20] and the double diffractive cross-section has been measured by [21]. The acceptance corrected inelastic cross-section is

$$A\sigma_{p\bar{p}} = A_{SD}\sigma_{SD} + A_{DD}\sigma_{DD} + A_{HC}(\sigma_{p\bar{p}} - \sigma_{SD} - \sigma_{DD}),$$

$$A\sigma_{p\bar{p}} = 50.58 \pm 3.01 \text{ mb.}$$

TABLE V. Measured cross-sections for inelastic and diffractive events.

Final state	$\sigma$ (mb)
inelastic	$60.7 \pm 2.4$
single diffractive	$9.6 \pm 0.5$
double diffractive	$7.2 \pm 2.0$

### C. Comparison To Run I

Table VI compares the input parameters to the acceptance corrected cross-section for Run I and Run II. The major differences are

- a 5% increase in the inelastic-cross section,
- an increase in the diffractive fraction from  $\sim 16\%$  to  $\sim 22\%$  due to the increased DD cross-section,
- large changes in the diffractive acceptances, including larger errors, due to the inclusion of the latest minimum bias generators.

Table VI also lists the results of the acceptance weighted cross-section for Run I using consistent values for the cross-sections. The diffractive cross-sections have not been scaled since the scaling is insignificant with respect to the errors and the exact form of the scaling function for diffractive processes is unknown.

TABLE VI. Comparison of the cross-sections and acceptances between the Run II Luminosity Monitor and the Run I LØ detector that had almost equivalent geometric acceptance. The Run I corrected values correspond to cross-sections consistent with the Run II results.

Parameter	Run I	Run I corrected	Run II
Cross-sections			
Inelastic	$57.55 \pm 1.56$	$59.23 \pm 2.3$	$60.7 \pm 2.4$
Single diffractive	$9.57 \pm 0.43$	$9.6 \pm 0.5$	$9.6 \pm 0.5$
Double diffractive	$1.29 \pm 0.20$	$7.2 \pm 2.0$	$7.2 \pm 2.0$
Acceptances			
Hard Core	$0.97 \pm 0.02$	$0.97 \pm 0.02$	$0.982 \pm 0.0125$
Single diffractive	$0.15 \pm 0.05$	$0.15 \pm 0.05$	$0.313 \pm 0.137$
Double diffractive	$0.72 \pm 0.03$	$0.72 \pm 0.03$	$0.624 \pm 0.130$
$A\sigma_{p\bar{p}}$	$47.70 \pm 2.03$	$47.80 \pm 2.53$	$50.58 \pm 3.01$
inelastic acceptance, $A$	82.8	80.7	83.4

## V. EFFICIENCY

The main sources of inefficiency are events with insufficient energy deposited in the LM to assert the discriminators in the north and south arrays and mistiming due to resolution or background hits that cause the interaction vertex to be reconstructed outside the interaction point. Inefficiency due to misclassification of an inelastic collision as beam halo is discussed in Section VII.A. This leads to a factorization into three components

$$\epsilon_{\text{LM}} = \epsilon(\text{N}) \times \epsilon(\text{S}) \times \epsilon(\text{fz}),$$

where  $\epsilon(\text{N})$  and  $\epsilon(\text{S})$  are the efficiencies for the north and south discriminators and  $\epsilon(\text{fz})$  is the vertexing efficiency.

### A. Discriminator Efficiency

We determine if a particle was in the acceptance of an LM array by looking at the energy deposited in the calorimeter behind the LM array. The calorimeter consists of an inner uranium calorimeter with coverage extending to  $|\eta| < 3.1$  for detection of electromagnetic showers (EMC) and an outer liquid argon calorimeter with coverage extending to  $|\eta| < 5.2$  for detection of hadronic showers (FHC). Figure 9 is the energy in the calorimeter behind the north array when both the north and south discriminators fired in a zero-bias data sample. Zero-bias refers to events triggered by a random clock that is in phase with the beam crossing. Here, the energy sum is formed using the energy in all cells in the EMC with cell energy above 100 MeV and cells in the FHC with a cell energy above 200 MeV. Figure 10 is the same distribution when the south fired but the north did not. Two components are clearly visible, a high energy component similar to Fig. 9 and a low energy pedestal. We attribute the high energy component to events where particles were in the north acceptance but the north array did not fire, referred to as the north inefficient sample. We

attribute the pedestal to events where particles were not in the north acceptance, dominated by diffractive events. We consider all events in this histogram to contain inelastic collisions since the south array is asserted for every event. The fraction of events where the south array spuriously fires is less than 0.2% determined from the rates with and without beam.

The dominant systematic uncertainty is the parameterization of the pedestal. We perform three different extraction procedures to estimate the size of this error. First, to extract the two components we perform a binned maximum-likelihood fit to the north energy sum distribution. The inefficient sample is modeled as a threshold function

$$T(x) = Nx^\alpha e^{\beta x}.$$

The pedestal is modeled as a histogram taken from the data sample where both the north and south arrays did not fire. No events with a good primary vertex are found in the pedestal sample indicating that the contribution from inelastic collisions is minimal. Figure 11 displays the results of the fit. The fit yields an inefficient event sample of 20.6k events. Combining this with the sample of events where both the north and south arrays fired yields an efficiency range of

$$96.1\% < \epsilon(N) < 96.8\%,$$

where the range corresponds to variations on the functional form used to model the inefficient component. Further systematic studies are discussed below. The corresponding fit for the south inefficiency is shown in Fig. 12. We find

$$94.3\% < \epsilon(S) < 95.4\%.$$

Another method to extract the inefficient component involves only summing the energy behind the LM in the EMC. The EMC has very different noise characteristics than the FHC and the noise in the two systems is uncorrelated to some extent. So one expects a very different energy distribution.

The energy distribution in the EMC behind the north array when the south array is on is shown in Fig. 13. Again, we model the pedestal with a histogram taken from the sample where both the north and south arrays are off. To determine a lower limit on the size of the inefficient sample, we subtract the pedestal after normalizing the pedestal to the first energy bin. This is a lower limit since it assumes there are no inefficient events under the pedestal in the lowest bin. After subtracting the pedestal, we determine an upper limit on the inefficiency by fitting the high energy component with an exponential and extrapolating to zero, assuming no turn-on behavior. The area under the exponential is used as the upper limit. These limits allow us to bound the efficiencies to

$$96.6\% < \epsilon(N) < 97.2\%,$$

$$94.7\% < \epsilon(S) < 95.6\%,$$

which are consistent with the above results.

A third procedure to extract the inefficient component involves examining the log  $E$  distribution of the energy in the EMC behind the luminosity arrays. As shown in Fig. 14, this has very powerful discrimination between pedestal and inelastic samples. Here we also examine events with and without a primary vertex separately. Figure 15 shows various distributions for this procedure. The inefficient component is extracted using a fit to the distributions where again the pedestal is modeled as a histogram from the sample where neither the north or south arrays fired. The inefficient component is modeled as an exponentiated second order polynomial. The fit to the north distribution is shown in Fig. 16. This method yields efficiency ranges of

$$96.7\% < \epsilon(N) < 98.0\%,$$

$$95.2\% < \epsilon(S) < 96.5\%,$$

where the range corresponds to variations in the fitting functions.

We have performed a detailed analysis of the stability of these results for several other variations such as bin size, cell threshold, fitting range, data taking period, and bunch dependence. Including the variations due to the three separate fitting procedures, the size of the north inefficient sample is found to vary within a range of  $\pm 30\%$  around the median value. The south inefficient sample is found to vary within a range of  $\pm 25\%$  around the median value leading to efficiencies of

$$\epsilon(N) = (97 \pm 1)\%,$$

$$\epsilon(S) = (95 \pm 1.2)\%.$$

### B. Combined North and South Efficiency

We have determined the discriminator efficiencies above using data samples where the opposite array was asserted. If the efficiencies are uncorrelated, the total efficiency is the product of these two numbers. We test for correlations by recalculating the efficiencies independent of whether the opposite array fired. For the north array, this corresponds to adding the events where the north fired but the south did not fire into the numerator and denominator, i.e. the south inefficient samples extracted above. We estimate the contribution of inelastic events where neither array fired using the product of the nominal inefficiencies for the two arrays. These are added to the denominator. The new efficiencies are

$$\epsilon(N) = (97.1 \pm 1.0)\%,$$

$$\epsilon(S) = (95.2 \pm 1.1)\%.$$

One can see that there is almost no change in the efficiencies. This is expected. Since the single side efficiency is so high, there is nearly a complete overlap between the total inelastic sample and the inelastic sample that has at least one array asserted. For simplicity we therefore take the efficiency as the product of the two efficiencies given the other side fired

$$\epsilon(N) \times \epsilon(S) = 92 \pm 1.6\%.$$

### C. Classification Efficiency

Finally, we examine the efficiency for the event to be classified as inelastic once both the north and south arrays have fired. This sample contains true inelastic collisions and a small fraction of halo events that should have been classified as halo.

Figure 17 is the energy sum in the EMC behind the north array for events where both arrays fired but the event was not classified as inelastic (no-FastZ sample). Events classified as inelastic collisions are overlaid (good-FastZ sample). One can see an excess at low energy due to the halo contribution. We fit the two samples with exponentials in the high energy region and scale the good FastZ histogram so that the intercepts of the exponentials are equal. The area of the scaled good FastZ histogram then gives the inelastic component of the no-FastZ sample.

We find a classification efficiency of 98.9%. The same procedure applied to the south energy distribution yields 98.5%. A similar procedure yields 98.2–98.3% for different fit parameterizations. Taking the median value yields an efficiency of

$$\epsilon(\text{fz}) = 0.986 \pm 0.004.$$

Combining the efficiency for the two discriminators and classification yields a final efficiency of

$$\epsilon_{\text{LM}} = 90.9 \pm 1.8\%.$$

## VI. EFFECTIVE INELASTIC CROSS-SECTION

The final ingredients of the effective inelastic cross-section are

$$\sigma_{p\bar{p}} = 60.7 \pm 2.4 \text{ mb},$$

$$A\sigma_{p\bar{p}} = 50.58 \pm 2.27 \text{ mb},$$

$$\epsilon_{\text{LM}} = 90.9 \pm 1.8\%.$$

This gives an effective cross-section of

$$\sigma_{p\bar{p},\text{eff}} = 46.0 \pm 2.6 \text{ mb}.$$

Table VII lists the relative contributions to the error from the individual inputs. For variable  $x_i$  with error  $\delta_i$  this is defined as

$$\frac{1}{\delta_{\text{total}}^2} \left( \frac{\partial \sigma_{p\bar{p},\text{eff}}}{\partial x_i} \right)^2 \delta_i^2.$$

TABLE VII. Final input values for the effective inelastic cross-section and their relative contributions to the final error.

Input	value	contributed error
Cross-sections (mb)		
inelastic	$60.7 \pm 2.4$	56%
single diffractive	$9.6 \pm 0.5$	1.1%
double diffractive	$7.2 \pm 2.0$	5.2%
Acceptance		
Non-diffractive (HC)	$0.98 \pm 0.01$	3.0%
single diffractive	$0.31 \pm 0.14$	18%
double diffractive	$0.62 \pm 0.13$	9%
detector efficiency	$0.91 \pm 0.02$	8%

### A. Comparison with Run I

Table VIII lists the effective cross-sections for the Run II, Run Ia, and Run Ib data periods including a rescaling for the new inelastic and double-diffractive cross-sections. From these numbers, we can derive corrections to the central values and luminosity components of the errors ( $\delta$ ) for Run I cross-sections that were normalized using inelastic  $p\bar{p}$  collisions:

$$\frac{\sigma(\text{Run 1 corrected})}{\sigma(\text{Run 1 original})} = 0.998,$$

$$\frac{\delta(\text{Run 1a corrected})}{\delta(\text{Run 1a original})} = 1.280,$$

$$\frac{\delta(\text{Run 1b corrected})}{\delta(\text{Run 1b original})} = 1.275.$$

To factor the error into correlated and uncorrelated components we assume a 100% correlation between the physics cross-sections. The acceptances are based on very similar detector geometries and similar MCs leading to large correlations which we take to be 100%. The efficiencies are derived from different data sets using different procedures and are thus uncorrelated. The relative error can then be factored into

$$\frac{\delta(\sigma)}{\sigma}(\text{Run II}) = 0.060(\text{correlated}) \oplus 0.026(\text{uncorrelated}),$$

$$\frac{\delta(\sigma)}{\sigma}(\text{Run Ia}) = 0.053(\text{correlated}) \oplus 0.021(\text{uncorrelated}),$$

$$\frac{\delta(\sigma)}{\sigma}(\text{Run Ib}) = 0.053(\text{correlated}) \oplus 0.022(\text{uncorrelated}).$$

Since the same MC and input inelastic and diffractive cross-sections are used to calculate the effective inelastic cross-section by the CDF collaboration, this factorization is also valid for combinations of DØ and CDF cross-section measurements.

TABLE VIII. Effective inelastic cross-sections for various DØ Run periods. The new values correspond to using inelastic and diffractive cross-sections consistent with the Run II values.

Run period	original value	updated value
Run Ia	$45.32 \pm 2.02$ mb	$45.41 \pm 2.59$ mb
Run Ib	$43.27 \pm 1.95$ mb	$43.36 \pm 2.49$ mb
Run II		$46 \pm 3$ mb

## VII. RATE DEPENDENT CORRECTIONS

### A. Halo Correction

In the above efficiency calculations, we took care to always exclude events that were classified as halo. We now examine the classification of events that contain both inelastic collisions and beam backgrounds. We refer to these as *vetoed* events as shown in Fig. 18. As discussed above, inelastic collision remnants have approximately equal time-of-flight to the north and south arrays while halo events have a large asymmetry between the flight times. If beam halo accompanies a bunch that has an inelastic collision, the halo particles will strike the upstream LM array early leading to a halo classification. This is effectively a dead time that is proportional to the halo rate.

The probability that an inelastic collision occurs in a beam crossing is independent of any upstream interactions, just as the probability is independent of whether or not an interaction occurred in the previous turn. Therefore, the ratio of events with an interaction to the total number of crossings is equivalent to the ratio of vetoed events to the total number of halo events. This can be corrected for online using the scalar rates for events classified as halo,  $R(\text{halo})$ , and events classified as inelastic,  $R(\text{inelastic})$

$$R(\text{inelastic corrected}) = R(\text{inelastic})(1 + R(\text{p halo}) + R(\bar{\text{p}} \text{ halo})).$$

At higher rates, this is only the first order correction. The full correction is

$$R(\text{inelastic corrected}) = \frac{R(\text{inelastic}) - R(\text{p halo}) \times R(\bar{\text{p}} \text{ halo})}{(1 - R(\text{p halo})) \times (1 - R(\bar{\text{p}} \text{ halo}))}.$$

We have validated this correction by counting primary vertices in events that were classified as halo. We find that the number of halo events containing primary vertices is consistent with expectation for random overlap of halo particles with inelastic events.

### B. Single Sided Processes at High Luminosity

We have defined the acceptance as the fraction of interactions that have particles incident on both LM arrays. With multiple interactions per crossing, this is satisfied if one interaction fires both sides or if separate interactions fire opposite sides. This gives the acceptance a luminosity dependent correction for *single sided* processes. The single sided effective cross-section is given by

$$\sigma_{SS} = \sum_i A(SS)_i \sigma_i = 6.3 \text{ mb}$$

where  $A(SS)_i$  is the probability that a particular interaction only fires one array. For Pythia MC  $A(SS)_{HC} = 0.005$ ,  $A(SS)_{SD} = 0.782$ ,  $A(SS)_{DD} = 0.358$ .

The correction is most readily applied to the original Poisson probability that no interactions are measured and is given by

$$P(0) = e^{-\sigma_{p\bar{p},\text{eff}}\mathcal{L}} \times (2e^{(-\sigma_{SS}/2)\mathcal{L}} - e^{-\sigma_{SS}\mathcal{L}}).$$

The effects of the new inelastic cross-section and the two corrections as a function of luminosity are plotted in Fig. 19.

### C. Luminosity Dependent Baseline Shifts

A luminosity dependent baseline shift due to AC coupling of the PMT signals before discrimination was discovered in Summer 2004. This has a large effect on the instantaneous luminosity on the order of 5 to 10% at a luminosity of  $1 \times 10^{32}$  cm/s<sup>2</sup> but very little effect for average and integrated luminosities in typical running periods. The effect of this shift is less than one percent on the integrated luminosity for the entire data set recorded before September 2004. An error of 1% is added in quadrature to the overall error to account for this effect and the errors associated with the above corrections.

## VIII. CONCLUSIONS

We have measured the effective inelastic  $p\bar{p}$  cross-section into the DØ LM to be  $46 \pm 3$  mb. This number relates the measured LM counting rate to the instantaneous luminosity that is used to normalize most DØ cross-section measurements. The dominant contribution to the 6.5% uncertainty is the error in the measured inelastic  $p\bar{p}$  cross-section followed by our understanding of the kinematic distributions for diffractive processes. These errors can be reduced in the future with new measurements of the inelastic and diffractive cross-sections and with the accumulation of large diffractive data samples tagged using information from the DØ Forward Proton Detector.

We are grateful for the detailed examination of this work by the DØ luminosity editorial board members Brad Abbott, Andrew Brandt, Brian Cox, Richard Partridge, Vlada Simak, and Greg Snow (Chair). We thank the staffs at Fermilab and collaborating institutions, and acknowledge support from the Department of Energy and National Science Foundation (USA), Commissariat à l’Energie Atomique and CNRS/Institut National de Physique Nucléaire et de Physique des Particules (France), Ministry of Education and Science, Agency for Atomic Energy and RF President Grants Program (Russia), CAPES, CNPq, FAPERJ, FAPESP and FUNDUNESP (Brazil), Departments of Atomic Energy and Science and Technology (India), Colciencias (Colombia), CONACyT (Mexico), KRF (Korea), CONICET and UBACyT (Argentina), The Foundation for Fundamental Research on Matter (The Netherlands), PPARC (United Kingdom), Ministry of Education (Czech Republic), Natural Sciences and Engineering Research Council and WestGrid Project (Canada), BMBF and DFG (Germany), A.P. Sloan Foundation, Research Corporation, Texas Advanced Research Program, and the Alexander von Humboldt Foundation.

- 
- [1] L. Babukhadia for the DØ Collaboration, FERMILAB-CONF-02/239-E, ICHEP 2002 proceedings, 906 (2002).
  - [2] J. Womersley, FERMILAB-CONF-03/001-E (2003).
  - [3] C-C. Miao, FERMILAB-Conf-98/395-E (1998).
  - [4] J. Bantly *et al.*, FERMILAB-TM-1930 (1996).
  - [5] J. Bantly *et al.*, FERMILAB-TM-1995 (1997).
  - [6] E710 Collaboration, N.A. Amos *et al.*, Phys. Rev. Lett. **63**, 2784 (1989).
  - [7] E811 Collaboration, C. Avila *et al.*, Phys. Lett. **B445**, 419 (1999).
  - [8] CDF Collaboration, F. Abe *et al.*, Phys. Rev. **D50**, 5550 (1994).
  - [9] S. Klimenko, J. Konigsberg, T.M. Liss, FERMILAB-FN-0741 (2003).
  - [10] S. Eidelman *et al.*, Phys. Lett. **B592** 1 (2004).

- [11] The MBR and DTUJET results are based on an earlier study of the Run II LM acceptance by R. Partridge during the design of the LM detector.
- [12] T. Sjostrand *et al.*, Computer Phys. Commun. **135** 238 (2001).
- [13] G.A. Schuler, T. Sjostrand, Phys. Rev. **D49**, 2257 (1994).
- [14] R. Engel, Z. Phys. **C66** 203 (1995).
- [15] P. Aurenche *et al.*, Phys. Rev **D45** 92 (1992).
- [16] R. D. Field, eConf C010630, 501 (2001), hep-ph/0201192.
- [17] R. Engel, PHOJET v1.05c, University Siegen preprint 95-05, (revised Feb. 1997)
- [18] E710 Collaboration, N. A. Amos *et al.*, Phys. Lett. **B301** 313 (1993).
- [19] R Brun *et al.*, GEANT 3.21, CERN Report No. DD/EE/84-1 (1987)
- [20] CDF Collaboration, F. Abe *et al.*, Phys. Rev. **D50**, 5535 (1994).
- [21] CDF Collaboration, T. Affolder *et al.*, Phys. Rev. Lett. **87**, 141802 (2001).

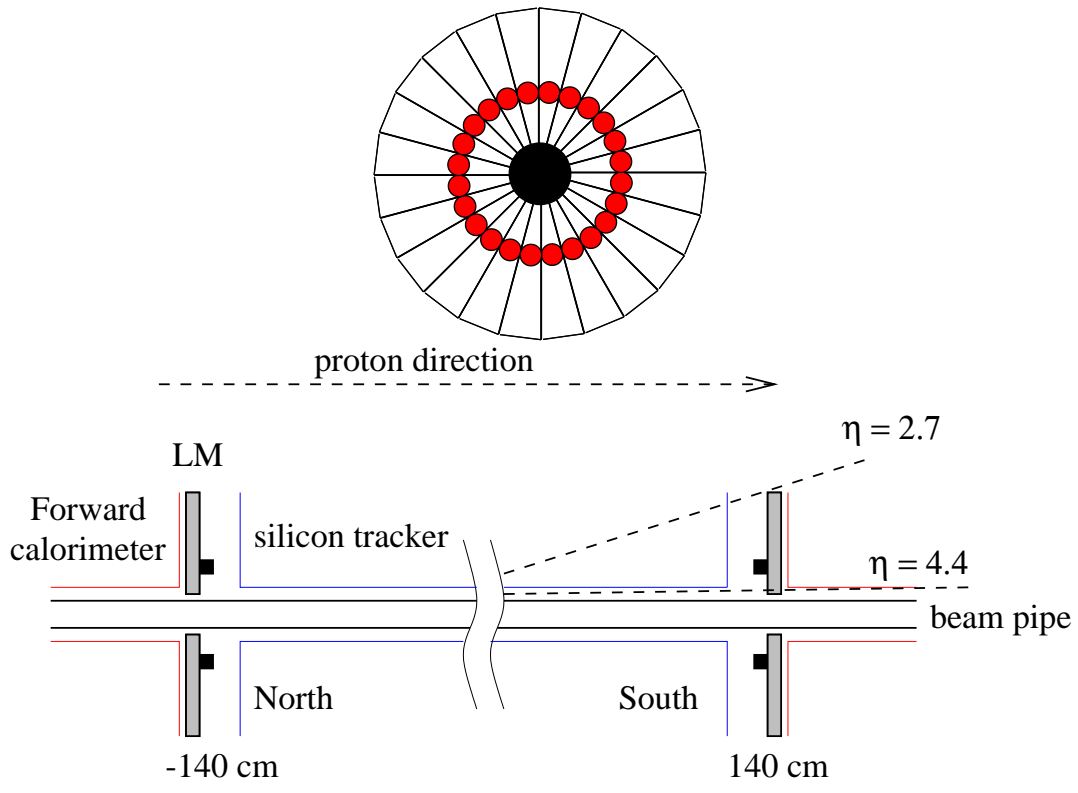


FIG. 1. Luminosity Monitor layout. The  $r-\phi$  view of one array is shown above. The  $r-z$  view of the two arrays is shown below.

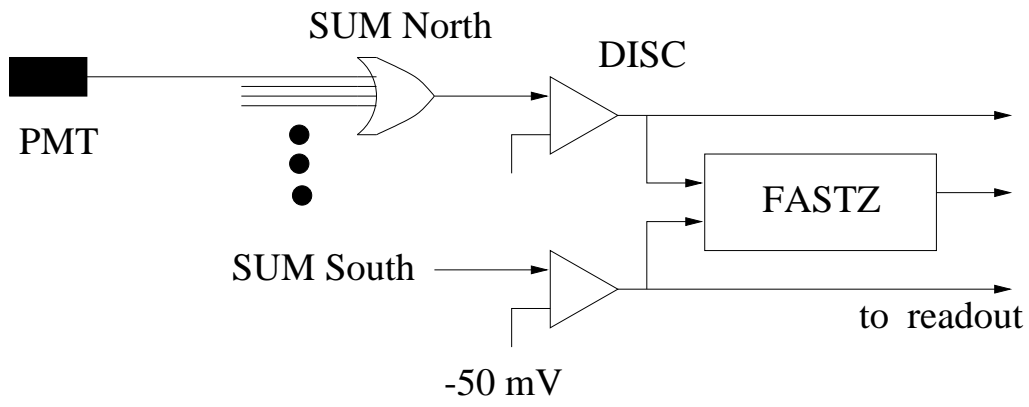


FIG. 2. Schematic of the LM signal processing.

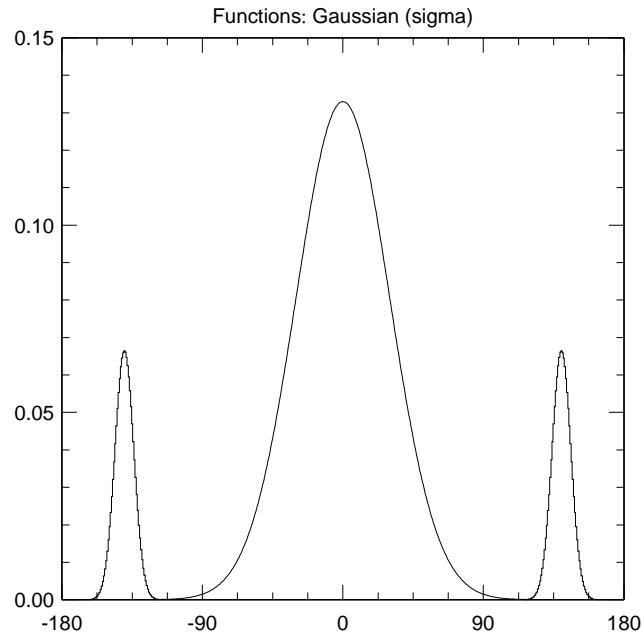
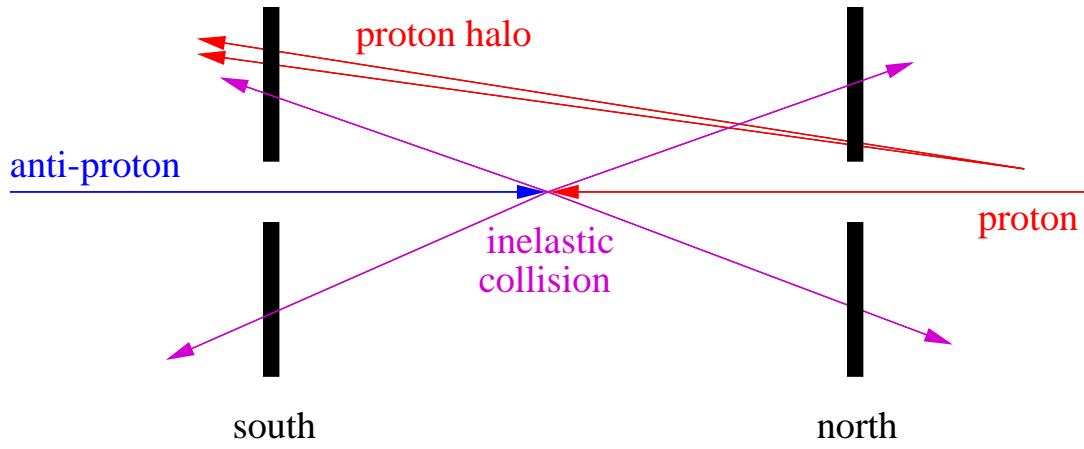


FIG. 3. Differentiation between inelastic collisions and beam halo using the  $z_{vtx}$  determination. The bottom figure shows the expected  $z_{vtx}$  distributions for inelastic collisions, centered at  $z_{vtx} = 0$  cm,  $p$  halo centered at  $z_{vtx} = -140$  cm and  $\bar{p}$  halo centered at  $z_{vtx} = 140$  cm.

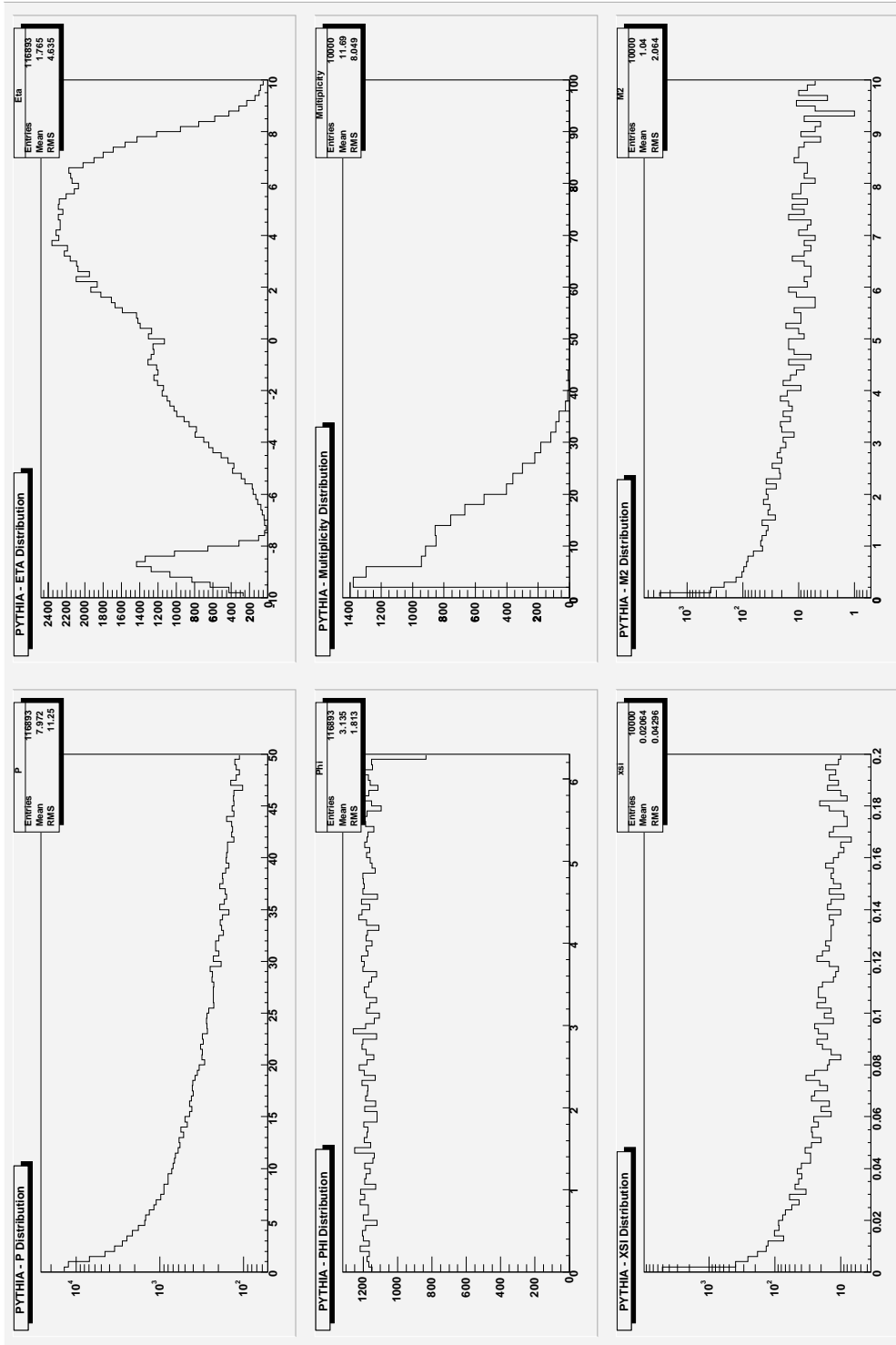


FIG. 4. Generator level kinematic distributions for single-diffractive events generated by Pythia. Landscape oriented top left: momentum, top right: pseudo-rapidity, center left: azimuthal angle, center right: charged particle multiplicity (all  $\eta$ ), bottom left: momentum transfer in the diffractive collision,  $\xi$ , bottom right: mass squared of the dissociated system.

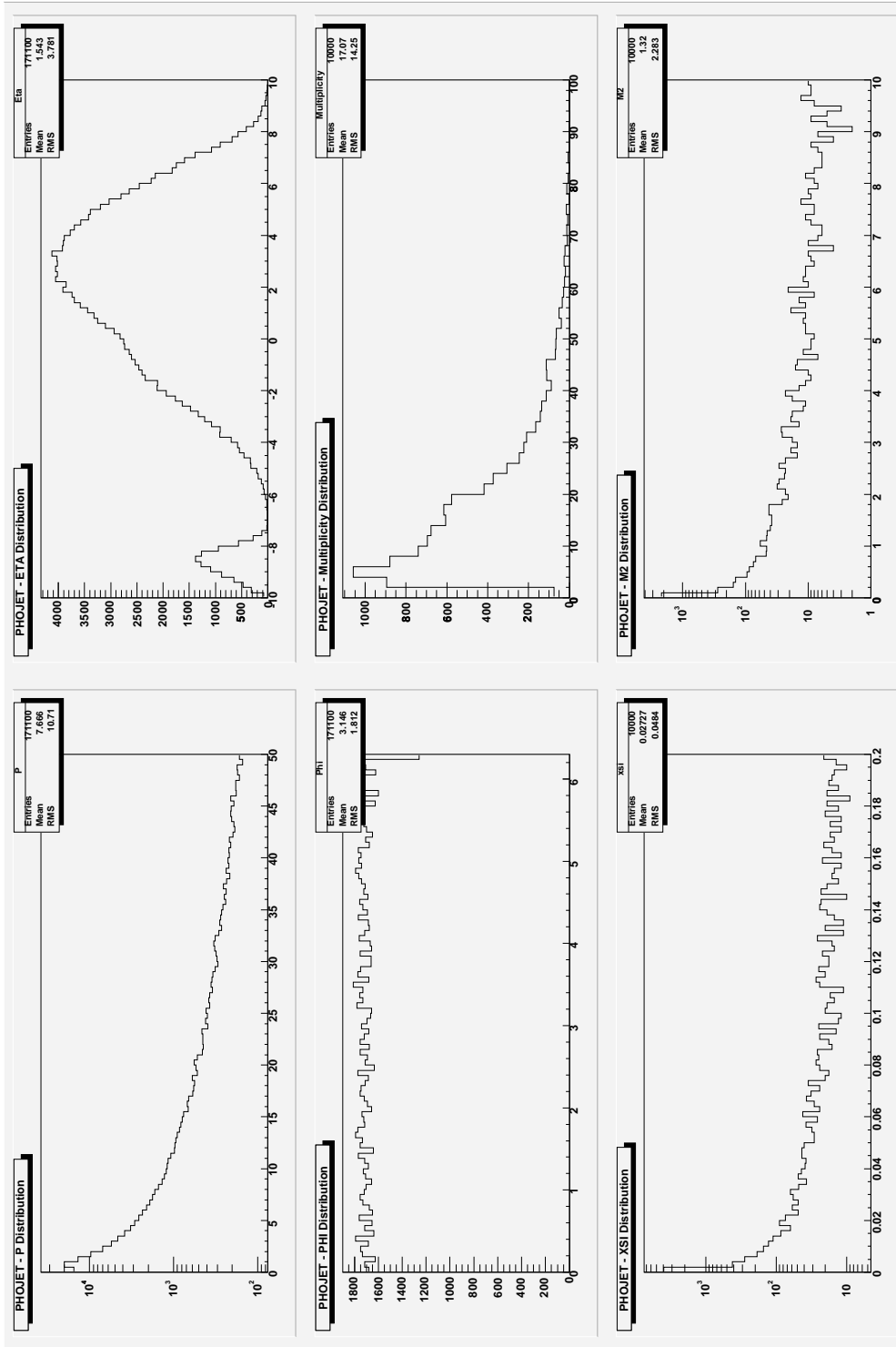


FIG. 5. Generator level kinematic distributions for single-diffractive events generated by PHOJET. Landscape oriented top left: momentum, top right: pseudo-rapidity, center left: azimuthal angle, center right: charged particle multiplicity (all  $\eta$ ), bottom left: momentum transfer in the diffractive collision,  $\xi$ , bottom right: mass squared of the dissociated system.

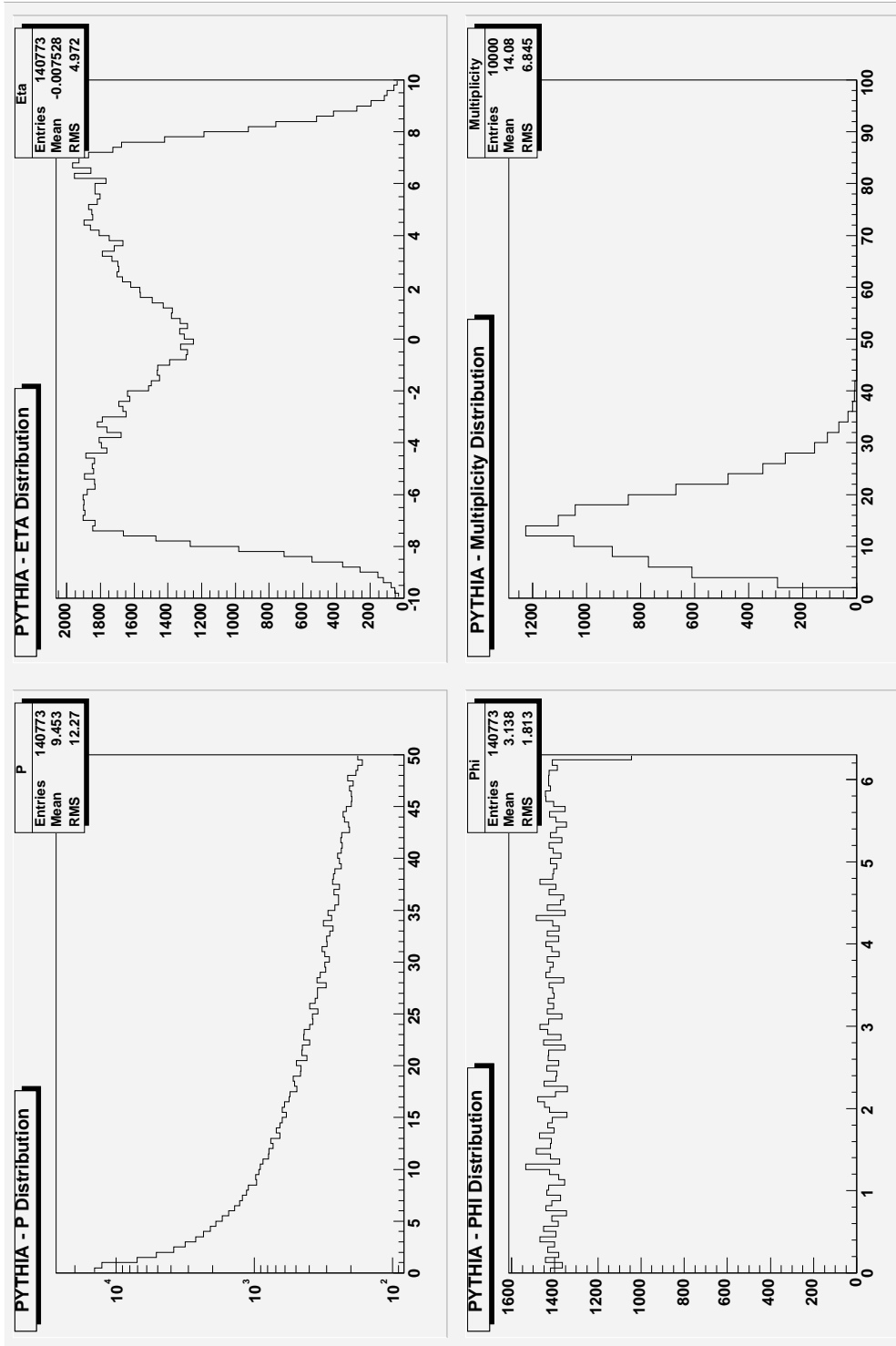


FIG. 6. Generator level kinematic distributions for double-diffractive events generated by Pythia. Landscape oriented top left: momentum, top right: pseudo-rapidity, bottom left: azimuthal angle, bottom right: charged particle multiplicity (all  $\eta$ ).

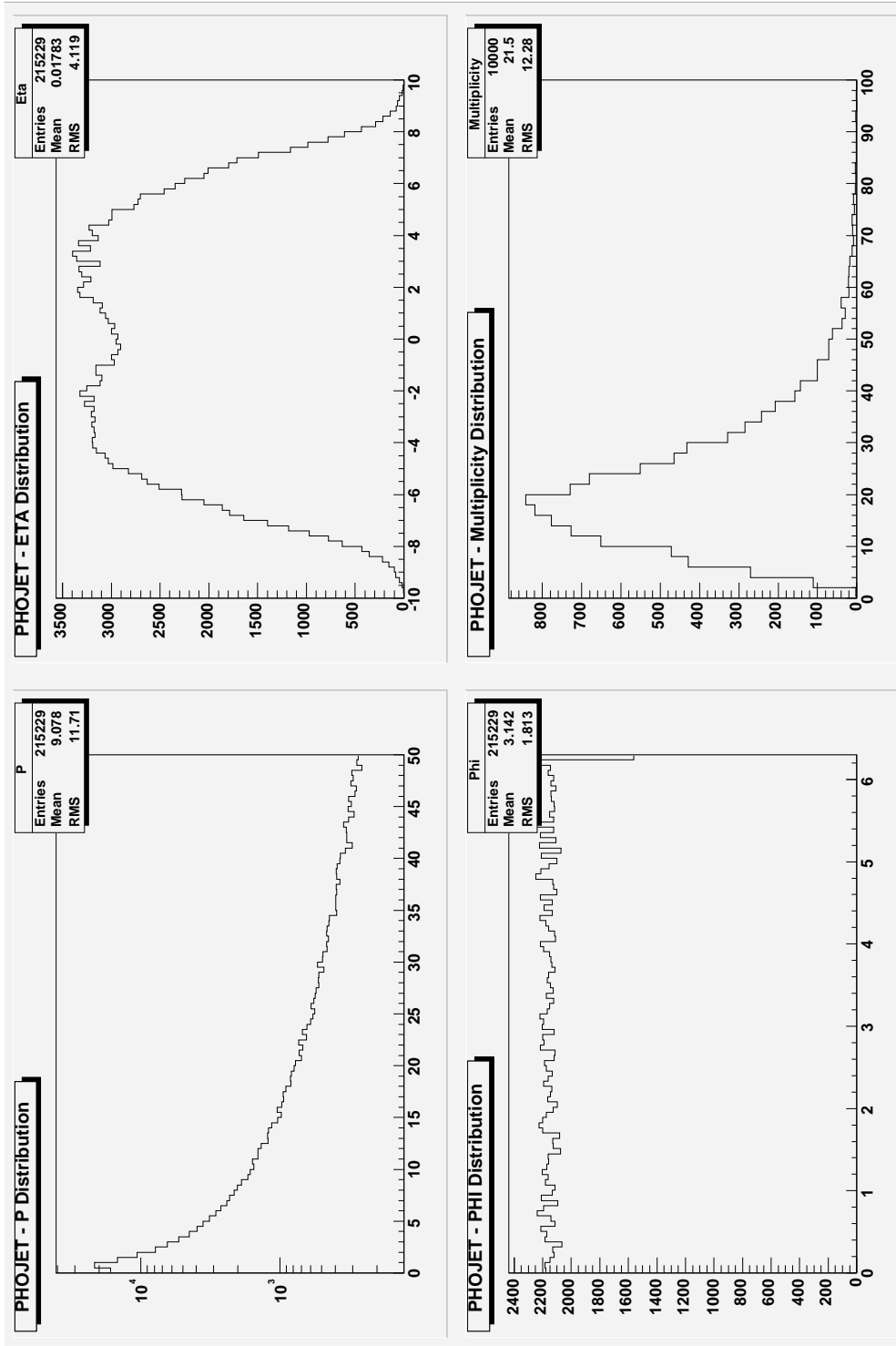


FIG. 7. Generator level kinematic distributions for double-diffractive events generated by PHOJET. Landscape oriented top left: momentum, top right: pseudo-rapidity, bottom left: azimuthal angle, bottom right: charged particle multiplicity (all  $\eta$ ).

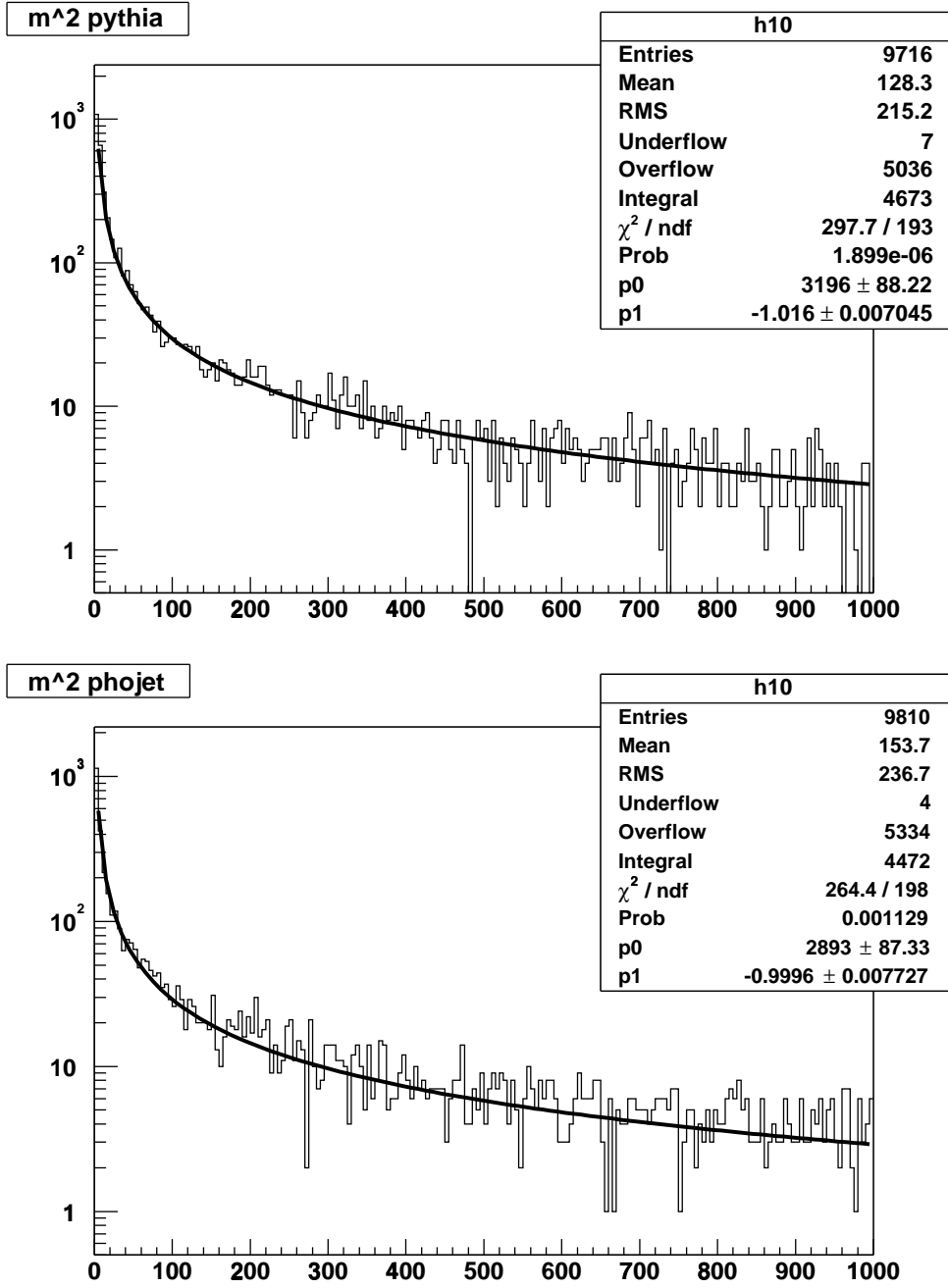


FIG. 8. Fits to the mass squared of the dissociated system in single-diffractive events generated by Pythia (top) and PHOJET (bottom). The parameter  $\alpha$  is given by -P1.

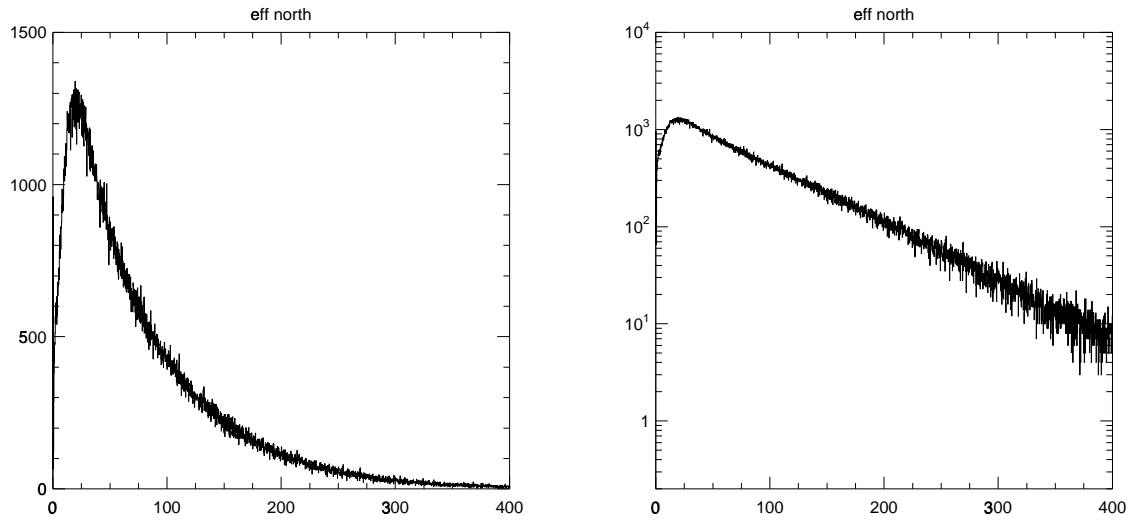


FIG. 9. Energy (GeV) behind the north LM array in the EM and FH calorimeters when the north and south discriminators are asserted.

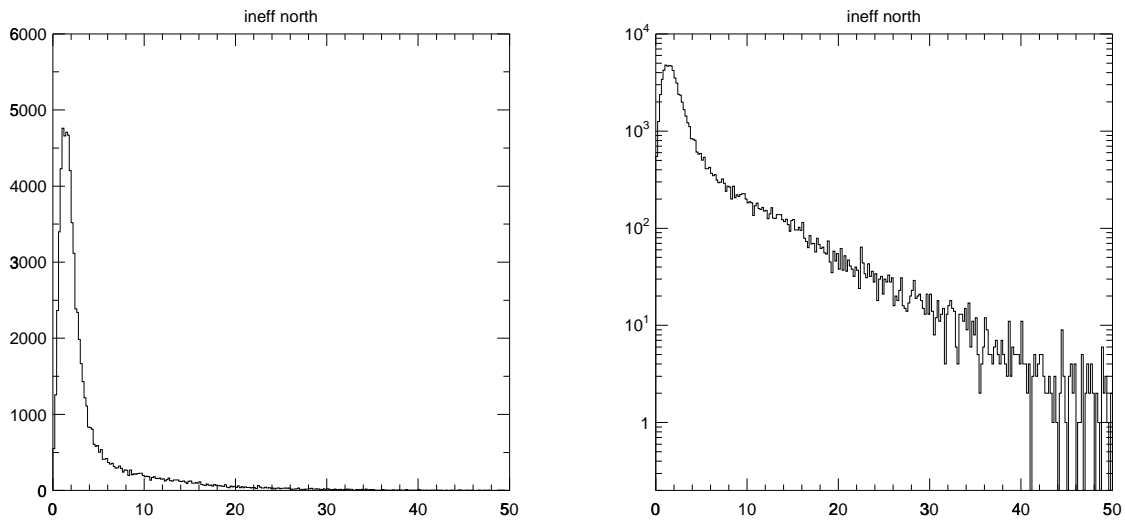


FIG. 10. Energy (GeV) behind the north LM array in the EM and FH calorimeters when both the north discriminator is off and the south discriminator is on.

MINUIT Likelihood Fit to Plot **2&100**

ineff north  
 File: hist/hists.plt  
 Plot Area Total/Fit 73025. / 72899. 16-DEC-2003 20:57  
 Func Area Total/Fit 72949. / 72899. Fit Status: 3  
 E.D.M.: 1.452E-07

Likelihood = 488.4  
 $\chi^2 = 518.0$  for 250 - 4 d.o.f., C.L.=0.168E-18%

Errors

Function 1: Histogram	1 100 Normal errors	Parabolic	Minos
NORM	6.32568E-02	$\pm 4.2550E-04$	- 4.2387E-04 + 4.2577E-04
Function 2: Threshold			
NORM	1845.6	$\pm 83.61$	- 83.52 + 83.05
* OFFSET	0.0000	$\pm 0.000$	- 0.000 + 0.000
POWER	0.36541	$\pm 2.8265E-02$	- 2.7381E-02 + 2.8918E-02
COEFF1	-0.15442	$\pm 2.4800E-03$	- 2.5094E-03 + 2.4336E-03
* COEFF2	0.0000	$\pm 0.000$	- 0.000 + 0.000

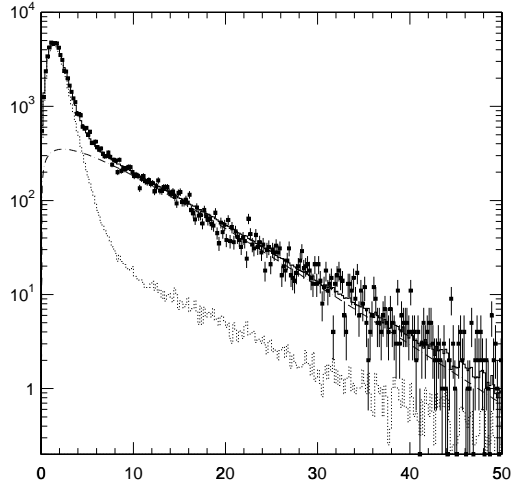
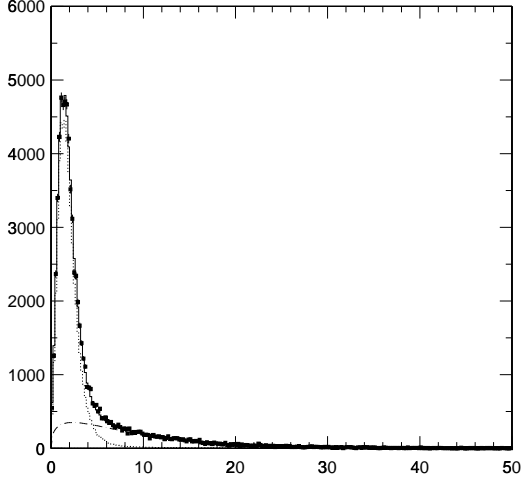


FIG. 11. Energy (GeV) behind the north LM array in the EM and FH calorimeters when the north discriminator was off and the south discriminator was on. The distribution is fit with a pedestal and a component for events that should have fired the discriminator.

MINUIT Likelihood Fit to Plot 5&100

ineff south  
 File: hist/hists.plt 16-DEC-2003 20:47  
 Plot Area Total/Fit 66950 / 66759 Fit Status 3  
 Func Area Total/Fit 66815 / 66759 E.D.M. 5.942E-07

Likelihood = 435.6  
 $\chi^2 = 473.0$  for 250 - 4 d.o.f., C.L.=0.163E-13%

Errors	Parabolic	Minos		
Function 1: Histogram	4 100 Normal errors			
NORM	4.30923E-02	$\pm 3.9538E-04$	- 3.9411E-04	+ 3.9574E-04
Function 2: Threshold				
NORM	2355.0	$\pm 82.39$	- 82.33	+ 82.04
* OFFSET	0.0000	$\pm 0.000$	- 0.000	+ 0.000
POWER	0.44577	$\pm 2.1724E-02$	- 2.1222E-02	+ 2.2108E-02
COEFF1	-0.15357	$\pm 1.8583E-03$	- 1.8752E-03	+ 1.8326E-03
* COEFF2	0.0000	$\pm 0.000$	- 0.000	+ 0.000

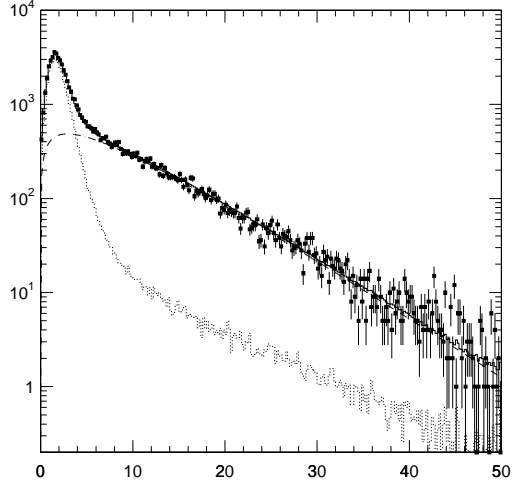
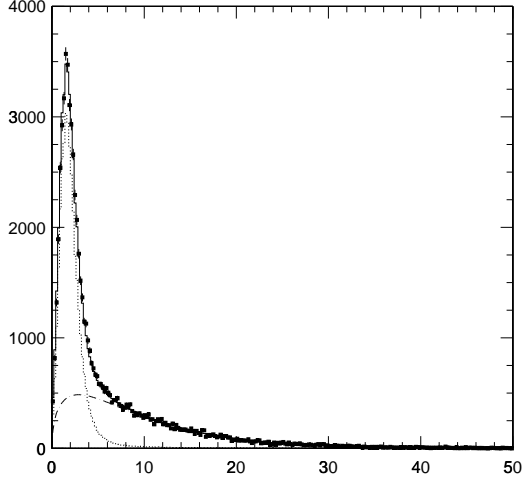


FIG. 12. Energy (GeV) behind the south LM array in the EM and FH calorimeters when the south discriminator was off and the north discriminator was on. The distribution is fit with a pedestal and a component for events that should have fired the discriminator.

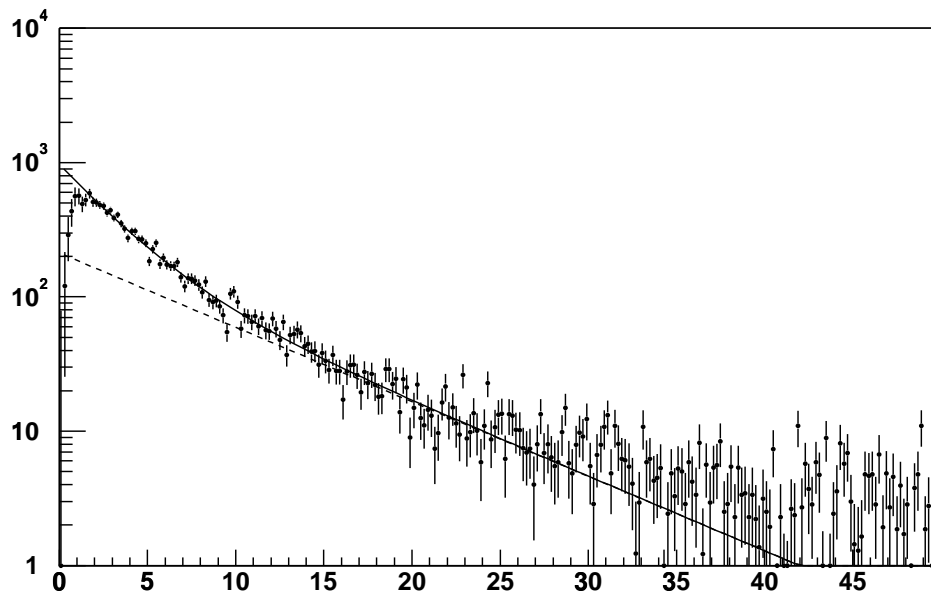
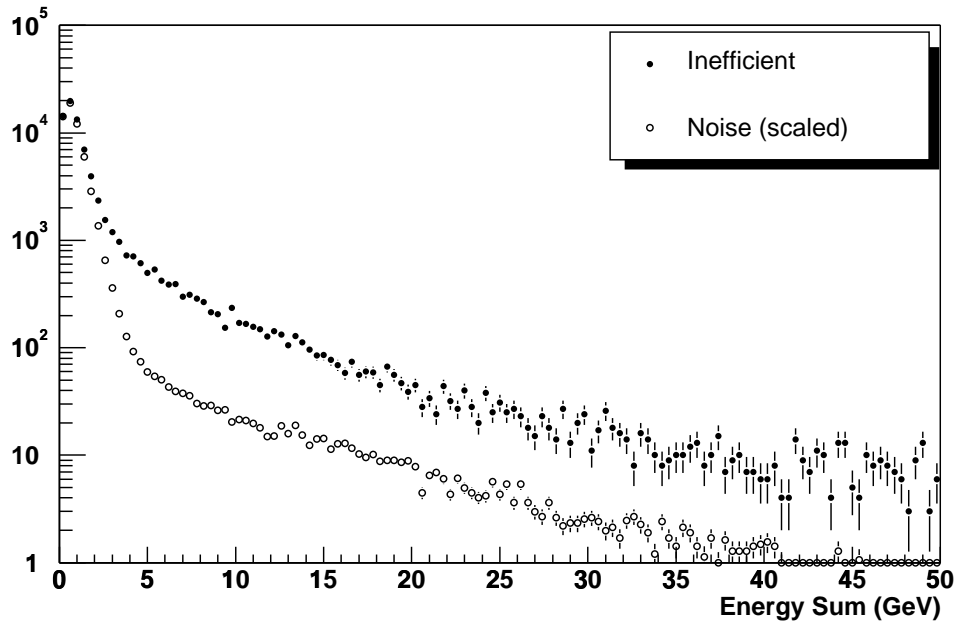


FIG. 13. Energy behind the north LM array in the electromagnetic calorimeter. In the top histogram, the solid points are events where the north LM array is not asserted but the south array is asserted. The open points are events where neither array is asserted scaled to the first so that the two distributions have equal entries in the first bin. The bottom histogram is the result of subtracting the above histograms. The distribution is fit with an exponential extrapolated to zero to estimate the possible effect of true inefficient events with zero energy.

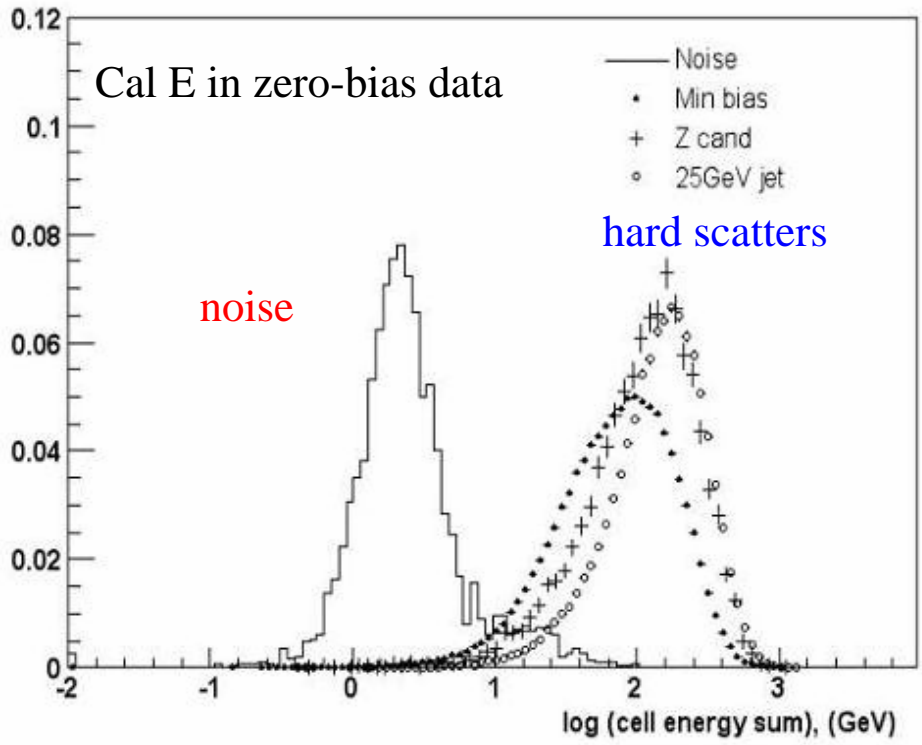


FIG. 14. Log Energy in the EM calorimeter behind the LM arrays. The solid line is data where both LM arrays are off. The black points are events classified as inelastic by the LM. The crossed points are  $Z \rightarrow \mu^+ \mu^-$  events. The open points are the events with at least one jet with energy greater than 25 GeV.

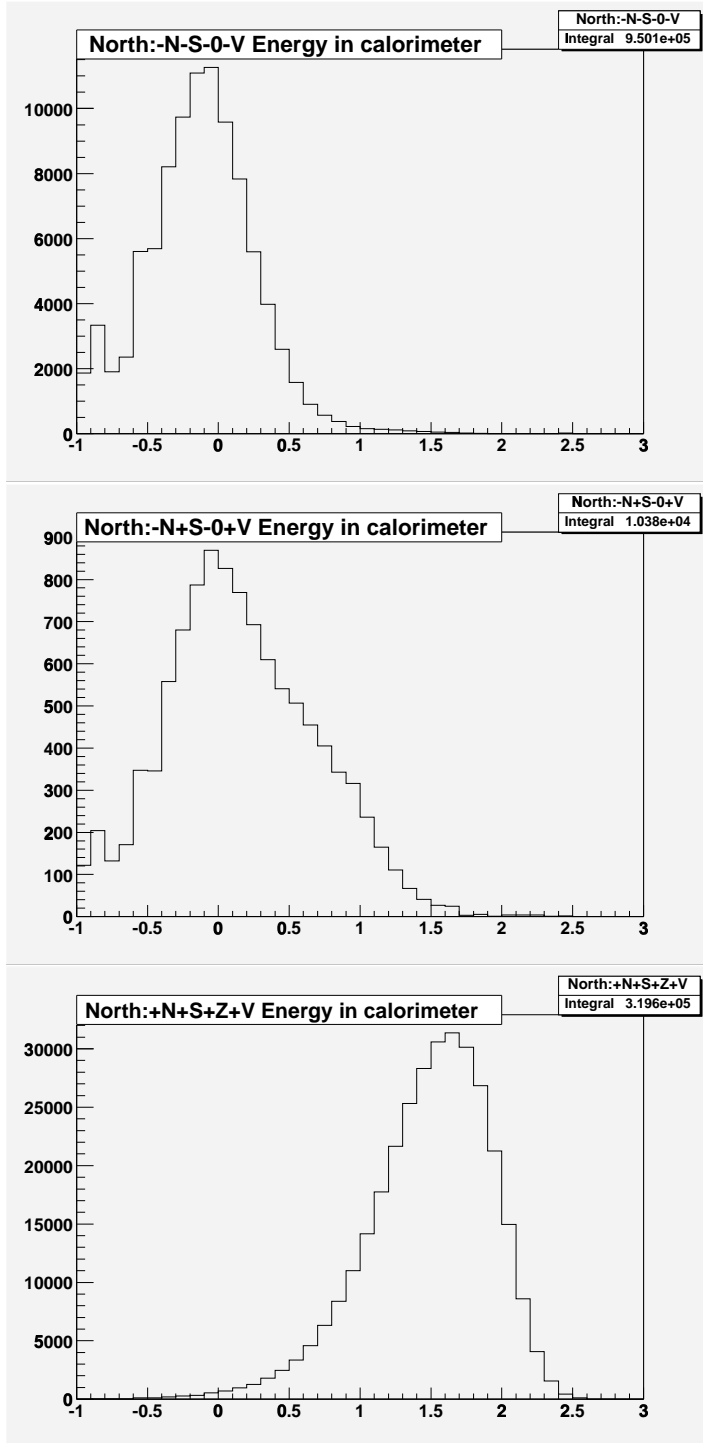


FIG. 15. Log Energy in the EM calorimeter behind the LM arrays. Top: Neither array is asserted and no vertex is reconstructed, center: energy behind the south array when the south array is asserted and the north array is not and a vertex has been reconstructed, bottom: energy distribution behind the north array for the same event sample as the center histogram.

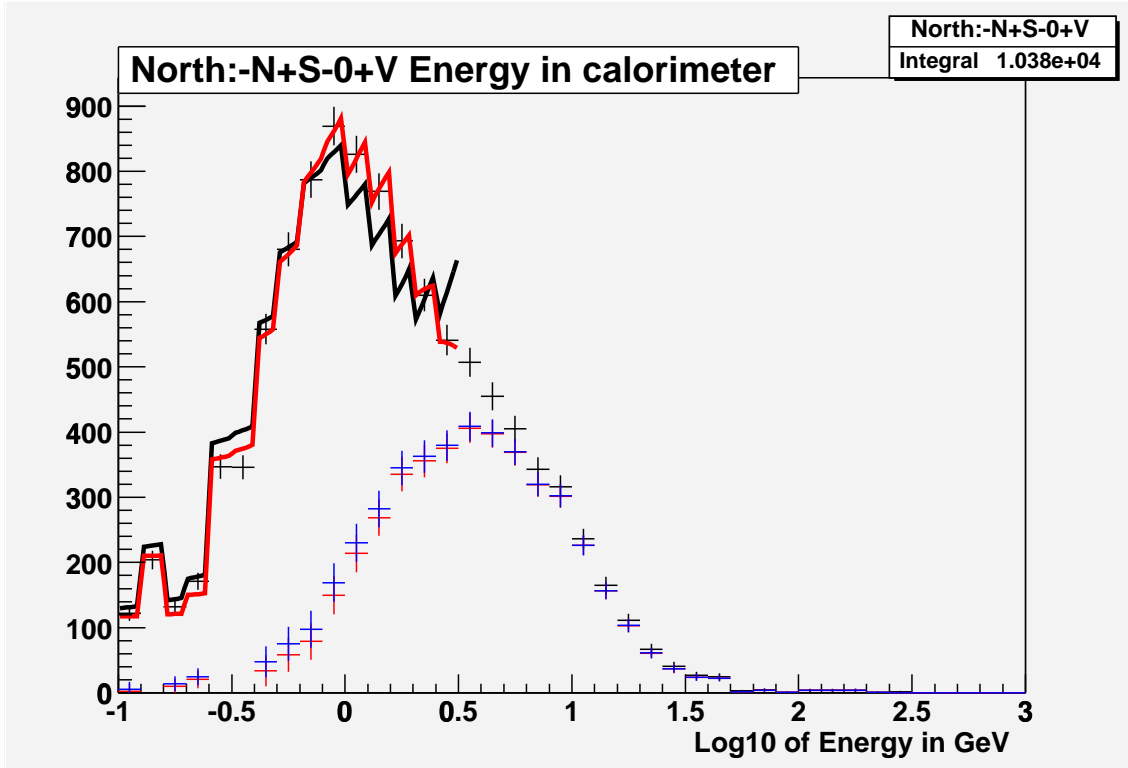


FIG. 16. Log Energy behind the north array for events where the south array is asserted and the north array is not and a vertex is reconstructed. The distribution is fit with a pedestal histogram taken from data and a Gaussian for events that should have fired the north array.

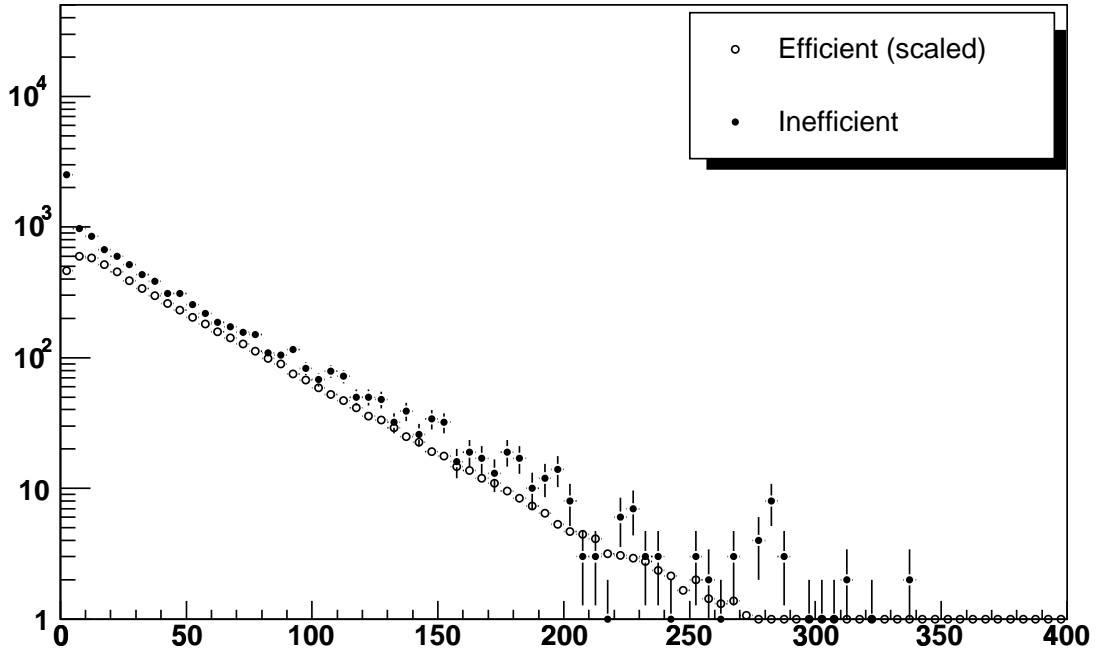


FIG. 17. Energy behind the north LM array in the electromagnetic calorimeter. The solid points are events where both LM arrays are asserted but the event is not classified as an inelastic collision. The open points are events classified as inelastic collisions. The two distributions are normalized to agree in the high energy region.

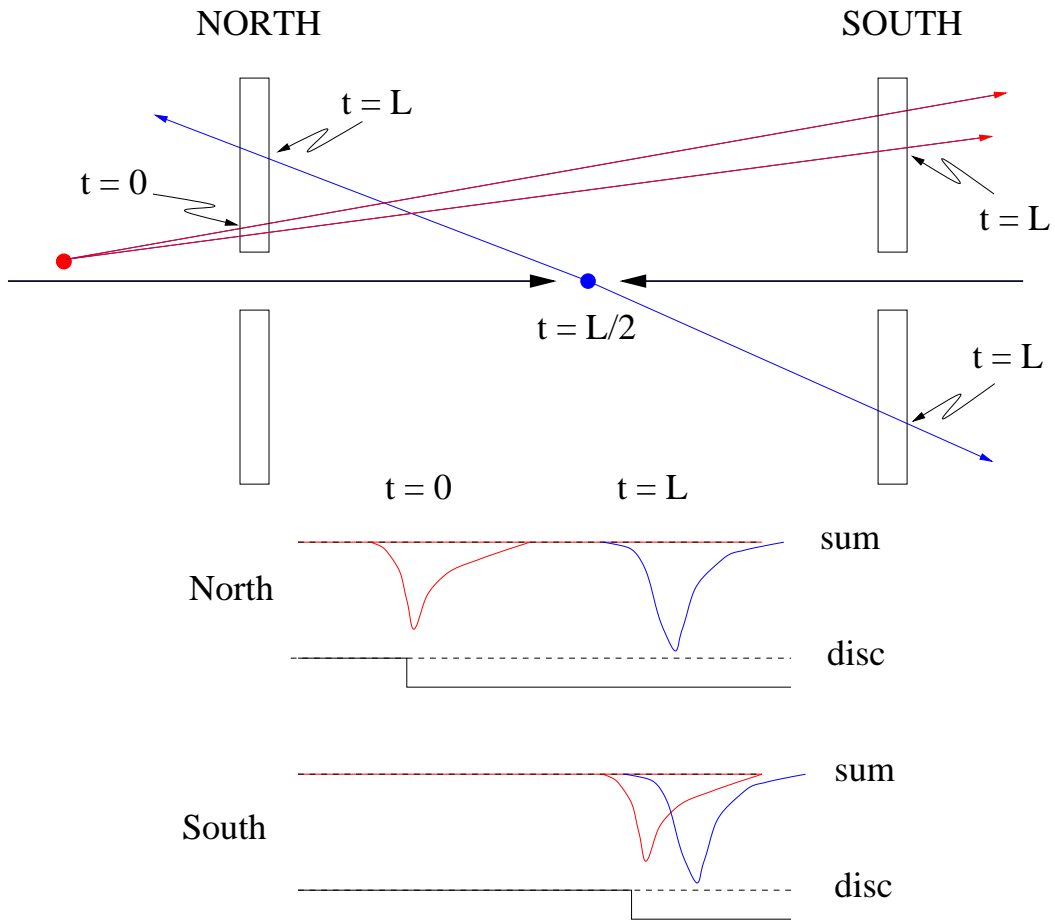


FIG. 18. Timing diagram for an event where both an inelastic collision and an upstream beam interaction occur.

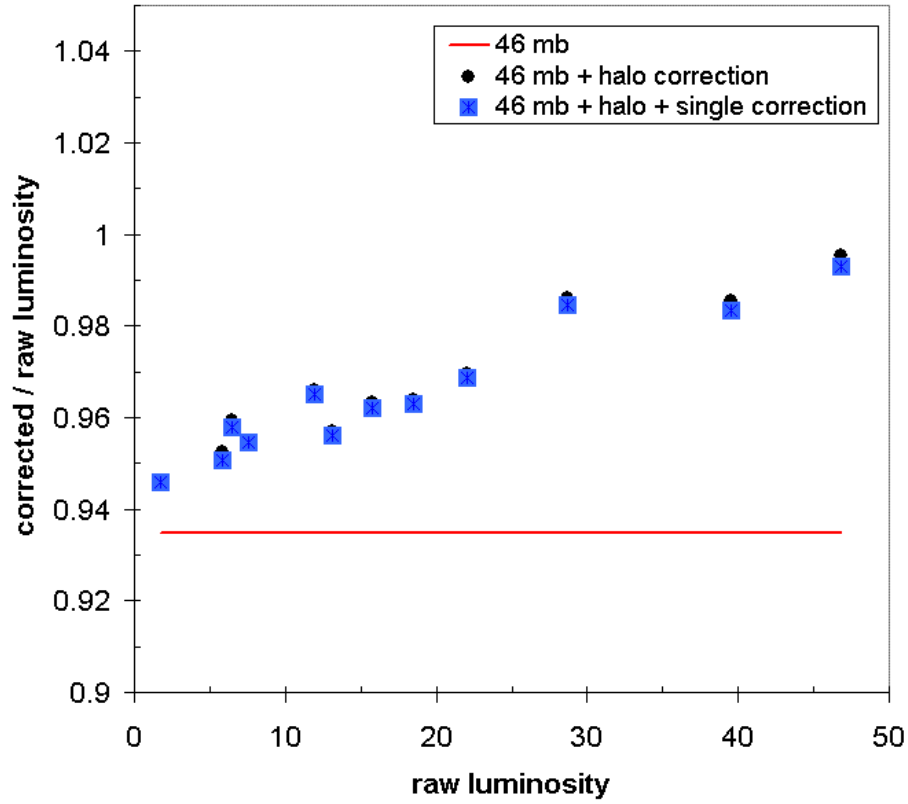


FIG. 19. Comparison of the updated effective inelastic cross-section to the previous value of 43 mb. The solid line indicates the shift due to increase to 46 mb. The circles and squares each correspond to the initial luminosity at the beginning of a particular store. The circles are the effect of the halo correction. The squares are the effect of the combined halo and single sided correction.